



## $sp^3$ -like defect structure of hetero graphene-carbon nanotubes for promoting carrier transfer and stability

Shan-Shan Fan<sup>a</sup>, Ling Shen<sup>a</sup>, Yuan Dong<sup>a</sup>, Ge Tian<sup>a,e,\*</sup>, Si-Ming Wu<sup>a</sup>, Gang-Gang Chang<sup>b</sup>, Christoph Janiak<sup>c</sup>, Ping Wei<sup>d</sup>, Jin-Song Wu<sup>d</sup>, Xiao-Yu Yang<sup>a,e,\*</sup>

<sup>a</sup> State Key Laboratory of Advanced Technology for Materials Synthesis and Processing, and School of Materials Science & Engineering, Wuhan University of Technology, Wuhan 430070, Hubei, China

<sup>b</sup> School of Chemistry, Chemical Engineering and Life Science, Wuhan University of Technology, Wuhan 430070, Hubei, China

<sup>c</sup> Institut für Anorganische Chemie und Strukturchemie, Heinrich-Heine-Universität Düsseldorf, 40204 Düsseldorf, Germany

<sup>d</sup> NRC (Nanostructure Research Centre), Wuhan University of Technology, Wuhan 430070, Hubei, China

<sup>e</sup> Department of Engineering and Applied Sciences, Harvard University Cambridge, MA 02138, United States

### ARTICLE INFO

#### Article history:

Received 14 June 2020

Revised 6 September 2020

Accepted 14 September 2020

Available online 19 September 2020

#### Keywords:

Graphene

Carbon nanotubes

$sp^3$ -like defect structure

Bio-electrocatalysis

Lithium-sulfur batteries

### ABSTRACT

Three-dimensional (3D) hybrid of nanocarbons is a very promising way to the high-performance design of electrocatalysis materials. However,  $sp^3$ -like defect structure, a combination of high strength and conduction of graphene and carbon nanotubes (CNTs) is rarely reported. Herein, 3D neural-like hybrids of graphene (from reduced graphene oxide) and carbon nanotubes (CNTs) have been integrated via  $sp^3$ -like defect structure by a hydrothermal approach. The  $sp^3$ -like defect structure endows 3D nanocarbon hybrids with an enhanced carrier transfer, high structural stability, and electrocatalytic durability. The neural-like structure is shown to demonstrate a cascade effect of charges and significant performances regarding bio-electrocatalysis and lithium-sulfur energy storage. The concept and mechanism of “ $sp^3$ -like defect structure” are proposed at an atomic/nanoscale to clarify the generation of rational structure as well as the cascade electron transfer.

© 2020 Science Press and Dalian Institute of Chemical Physics, Chinese Academy of Sciences. Published by ELSEVIER B.V. and Science Press. All rights reserved.

## 1. Introduction

Hybrids dictate the performance of nanocarbons as emerging renewable energy conversion technology [1–3]. The neural network of our brain is a high efficiency hybrid system of a three-dimensional (3D) cascade charge transport/collection and it therefore inspires the search for the design of 3D hybrids of nanocarbons for an anticipated performance in electrocatalysis [4–6]. However, the chemically weak linkages of graphene (G) and carbon nanotubes (CNTs) often lead to a low structural stability of 3D G/CNTs hybrids and a low out-of-plane conductivity, which greatly limits their practical applications [7–10]. The  $sp^2$  bonded carbon atoms are the most thermodynamically stable form of graphene and CNTs, and therefore a high strength  $sp^2$  C–C bond between the CNTs and graphene is theoretically as well as

technologically difficult [11]. The  $sp^3$  hybridized orbital is another type of C–C covalent bond for constructing a stable 3D atomic phase such as diamond. However, these have a low conduction due to lack of free electrons in four  $sp^3$  orbitals [12]. The  $sp^3$ -like defect structure (mainly bridged and folded interface carbon, Fig. S1a) would significantly change the properties of the surrounding  $sp^2$  network, particularly the electrochemical activity and the electronic conductivity [13,14]. Note that “ $sp^3$ -like defect structure” is only a predictive model to describe the strong interaction of nanocarbons. To our best knowledge, there is no experimental verification of “ $sp^3$ -like defect structure” on graphene and CNTs for activity promotion and stability enhancement in practical use, e.g. electrochemical applications.

During the hydrothermal reduction, the synthesis of a G/CNTs couple, attributed to the –OH and –COOH groups of the carbon surfaces, could create  $sp^3$ -like defect structures (Fig. S1b) [15–17]. Very interestingly, with the formation of bridge bonding, the graphene sheets could intimately contact with the CNTs and folds would occur, leading to the formation of more  $sp^3$ -like defect structure. Herein, we employed rich oxygen-containing graphene oxide (GO) with carboxylated multi-walled CNTs as raw materials to

\* Corresponding authors at: State Key Laboratory of Advanced Technology for Materials Synthesis and Processing, and School of Materials Science & Engineering, Wuhan University of Technology, 430070 Wuhan, Hubei, China (X.-Y. Yang).

E-mail addresses: [gtian@seas.harvard.edu](mailto:gtian@seas.harvard.edu) (G. Tian), [xyyang@seas.harvard.edu](mailto:xyyang@seas.harvard.edu), [xyyang@whut.edu.cn](mailto:xyyang@whut.edu.cn) (X.-Y. Yang).

synthesize neural-like 3D graphene-carbon nanotubes hybrids (3D G-C) with  $sp^3$ -like defect structure under a hydrothermal process. Nanofusions can be detected by TEM, and the clear increase of  $sp^3$ -like defect structure in the data of NMR, Raman and XPS, demonstrates that  $sp^3$ -like defect structure is formed in the hybrids of graphene and CNTs, which show significant performance enhancement in bio-electrocatalysis and electrochemical energy storage.

## 2. Experimental

### 2.1. Materials

The graphite (325 mesh), sulfur (100-mesh particles), and carboxylated multi-walled carbon nanotubes (CNTs) were purchased from Aladdin (China). The glucose oxidase (GOD) (Type X-S from *Aspergillus Niger*, 100000–250000 U g<sup>-1</sup> solid), disodium hydrogen phosphate dodecahydrate (Na<sub>2</sub>HPO<sub>4</sub>·12H<sub>2</sub>O), sodium dihydrogen phosphate (NaH<sub>2</sub>PO<sub>4</sub>) and *N,N*-Dimethylformaldehyde (DMF) were purchased from Aladdin (China). Sublimated sulfur was purchased from Sigma-Aldrich. The electrolyte of the Li-S batteries was 1.0 M lithium bis(trifluoromethanesulfonyl)imide (LiTFSI) dissolved in dimethoxymethane/1,3-dioxolane (DME/DOL, 1/1, v/v) with 1.0 wt% LiNO<sub>3</sub>.

### 2.2. Preparation of GO, 3D G-C, mixed G-C, 3D rGO and CNTs

Graphene oxide (GO) was prepared through the modified Hummers method [18,19]. The dispersion was centrifuged and washed with 300 mL of dilute hydrochloric acid (hydrochloric acid:water = 1:9, volume ratio) and then washed repeatedly with deionized water to a pH value of 5–6. Finally, dispersing the product in deionized water, a yellow-black GO dispersion was obtained. A freeze-dried 10 mL GO dispersion was used to obtain the dried powder (the quality of GO powder is recorded as “m”), and the dispersion concentration was calculated through the following formula:  $c$  (mg/mL) =  $m/10$ . The resulting GO dispersion was diluted to 1.5 mg mL<sup>-1</sup>. The amount of 30 mg CNTs was added in 40 mL 1.5 mg mL<sup>-1</sup> GO dispersion. Then the mixture was stirred, sonicated and then put into Teflon-line sealed autoclave and kept at 180 °C for 12 h. We obtained three-dimensional (3D) columnar hydrogel composites. And the composite was freeze-dried to obtain powdered 3D graphene-CNTs (3D G-C). As control groups, single component of GO and carboxylated multi-walled CNTs was transformed into 3D rGO and CNTs through the same hydrothermal process (the same concentration of dispersion was stirred, sonicated and then put into Teflon-line sealed autoclave and kept at 180 °C for 12 h), respectively. Additionally, the mixed G-C was obtained through mechanical mixing the above 3D rGO and CNTs with 1:1 mass ratio because of removal of rich oxygen-groups.

### 2.3. Preparation of enzyme electrodes

10 mg of GOD was dissolved into 1 mL of PBS (including Na<sub>2</sub>HPO<sub>4</sub>·12H<sub>2</sub>O and NaH<sub>2</sub>PO<sub>4</sub>, pH = 7). Then, 10 mg of the prepared powder (3D G-C, Mixed G-C, CNTs and 3D rGO) was evenly dispersed in 1.0 mL of DMF through sonicating for 30 min. The above-mentioned enzyme solution and powder dispersion were mixed, and allowed to store at 0–4 °C for 24 h. Then, 10 μL of the mixture was dropped onto a glassy carbon electrode. Notably, the glassy carbon electrode with active materials was fixed with 10 μL of 0.5% Nafion solution after drying at room temperature. Finally, we obtained 3D G-C@GOD enzyme electrodes. 3D

rGO@GOD, CNTs@GOD and mixed G-C@GOD enzyme electrodes were prepared for comparison by the same procedure.

### 2.4. Preparation of Li-S batteries

The 3D G-C material was first mixed with sulfur (S) powder with a mass ratio of 3:7 and grinded for 30 min; then mixture was placed in Teflon-lined autoclave at 155 °C for 12 h to incorporate the S into the 3D G-C for fabrication of S@3D G-C. Using the same method, we prepared S@3D rGO, S@mixed G-C and S@3D CNTs. Fresh lithium foil was employed as counter and reference electrodes and Celgard 2400 was employed as the separator of the Li-S batteries. The working electrode was composed of active material (S@3D G-C), acetylene black and polyvinylidene fluoride (PVDF) with a mass ratio of 7:2:1, where *N*-methyl pyrrolidinone (NMP) was used as dispersion liquid. The above raw materials were mixed evenly into slurry and coated on the surface of aluminum foil with sulfur mass loading about 1.0 mg cm<sup>-2</sup>. The volume of the electrolyte is about 15 μL mg<sup>-1</sup> in each coin cell. The assembly process of the coin cells was carried out in an argon atmosphere glove box. As comparison, we also assembled coin cells with the active materials of S@3D rGO, S@mixed G-C and S@CNTs.

### 2.5. Characterizations and measurements

Scanning electron microscopy (SEM, Hitachi S-4800) and transmission electron microscopy (TEM, JEOL-2100F) were employed to analyze the morphology of the as-prepared materials. The crystal structure information of the materials is tested by X-ray diffraction (XRD; Bruker D8 Advance) with Cu K $\alpha$  radiation ( $\lambda = 1.5418$  Å). The nitrogen sorption isotherms were measured through Micromeritics ASAP 3020 system. X-ray photoelectron spectroscopy (XPS) measurements of materials were conducted on PHI Quantera II (ULVAC-PHI). Raman spectra were collected using an Invia Raman Microscope with Nd YAG laser wavelength of 632.8 nm. <sup>13</sup>C HPDEC MAS nuclear magnetic resonance (NMR) experiments were carried out on Bruker AVANCE-III 400 spectrometer (MAS probe: 4 mm) with a sample spinning rate of 10 kHz, a 13C  $\pi/2$  pulse length of 4 μs and a recycle delay of 3 s. Atomic force microscopy (AFM) data were obtained by a Bruker-Catalyst at a frequency of 1 Hz. The TGA analysis was measured on Labsys Evo (Setaram) instrument with a ramp rate of 5 °C min<sup>-1</sup> in nitrogen atmosphere. UV-visible spectra of materials were tested on a UV-visible spectrophotometer (UV-2550). Fourier transform-infrared (FT-IR) spectra were tested on a Vertex 80 V (Bruker) spectrometer with KBr pellet technique in the range of 1300–2000 cm<sup>-1</sup>. The cyclic voltammetry (CV) curves of enzyme electrodes (three-electrode system) and Li-S batteries (0.2 mV s<sup>-1</sup>, 1.4–2.8 V) were obtained through electrochemical workstation (CHI 660D). The galvanostatic charge/discharge tests of the Li-S batteries were carried out on a LAND CT2001A System (1.4–2.8 V). Electrochemical impedance spectroscopy (EIS) was collected at Autolab PGSTAT 302 N in the frequency range of 10<sup>5</sup>–10<sup>-2</sup> Hz.

## 3. Results and discussion

As exhibited in Fig. 1(a,b), the 3D G-C hybrids reveal a 3D interconnected ellipsoidal brain-like and porous network with a long axis and short axis size of approximately 6–8 μm and 3–4 μm, respectively. A unique neural model structure that the graphene sheets (Fig. S2) act as joints for carrier collection and the CNTs seem like neurofibrils link in the different linkages (Fig. 1c). Fig. 1(d) shows that the head of the CNTs is entrapped into the graphene sheet and the folded structure in graphene mainly occurs

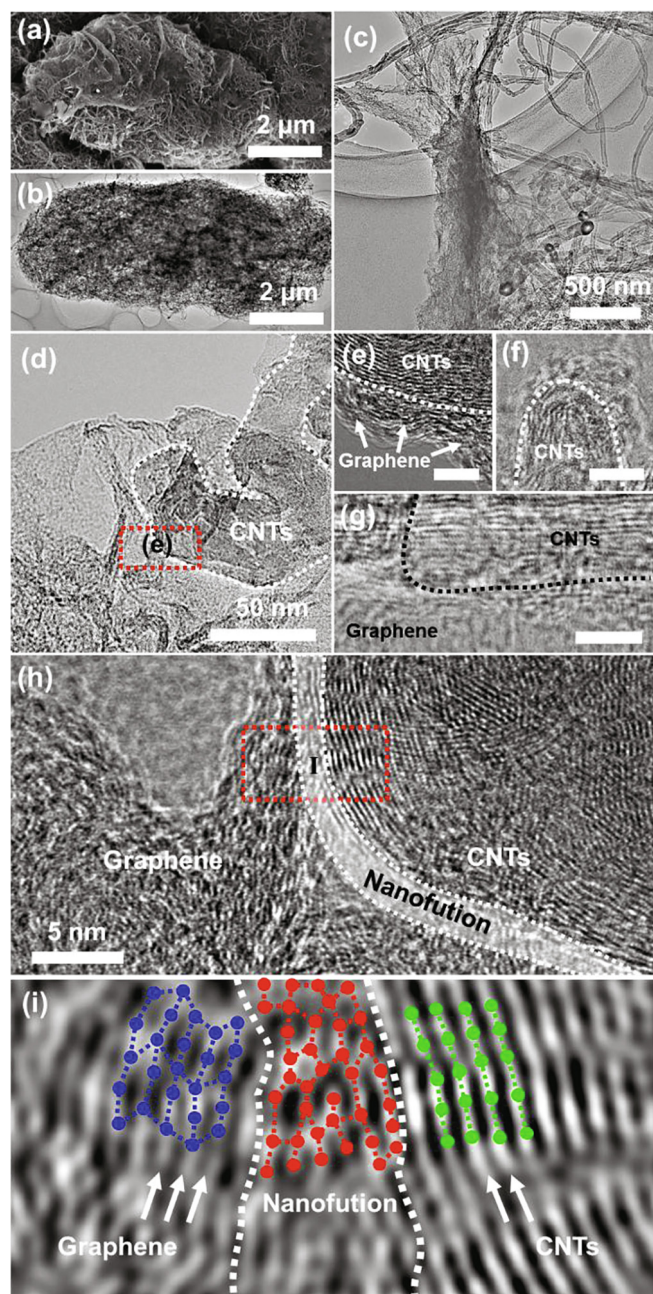


**Fig. 1.** (a) SEM image of 3D G-C. (b–d) TEM images of 3D G-C. (e–g) High resolution TEM images of 3D G-C (The rectangular scale in (e,g) is 2 nm in length). (h) High resolution TEM image of 3D G-C (the white belt in (h) is used to distinguish the nanofusion of the interface). (i) Inverse FFT image of region I, the corresponding atomic models of graphene (blue, left), nanofusion phase (red, middle) and CNTs (green, right).

around the CNTs. The pure carboxylated CNTs will not self-assemble into a 3D structure (Fig. S3a,b) and only GO will form a 3D foam-like structure during hydrothermal treatment, though not an individual core-shell structure (Fig. S3c,d). As shown in Fig. 1(e–g) (the original HRTEM images are shown in Fig. S4.), folded structures of graphene around the CNTs include ripple-like (Fig. 1e), square-like (Fig. 1f), and long-range encapsulation (Fig. 1g). Fig. 1(h) shows the interfacial nanofusion of graphene and CNTs, having obvious order-disorder-order arrangements [20,21]. Further the magnifying images of region I in Fig. 1(h) (Fig. 1i, the original images are shown in Fig. S5) indicated that the lattice fringes of graphene are well merged with lattice fringes

of the CNTs suggesting their highly integrated nanostructure, and the atomic position of the interface between graphene and CNTs are twisted, representing the nanofusion between graphene and CNTs. The lattice of nanofusion surely seems like deformation. This might be due to the relatively strong interaction among rGO sheets and CNTs and nonvertical projection of 3D structure.

As shown in Fig. 2(a), a diffraction peak at  $2\theta = 11^\circ$  without other peaks confirm the successful fabrication of GO. And this represents the interlayer spacing is 7.5 Å, which is due to the intercalation of –OH and –COOH containing functional groups between the graphene layers [22]. The XRD patterns of the other samples exhibit two main peaks at  $26.4^\circ$  (corresponding to the (002) plane of graphite with interlayer separation of 3.37 Å) and  $42.4^\circ$  (corresponding to the (100) plane) [23,24]. The peak position of GO changes to the 3D rGO via the hydrothermal process, indicating a reduction process and removal of the oxygen groups [25]. SEM

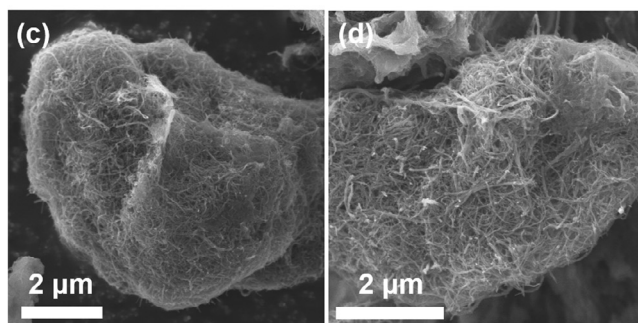
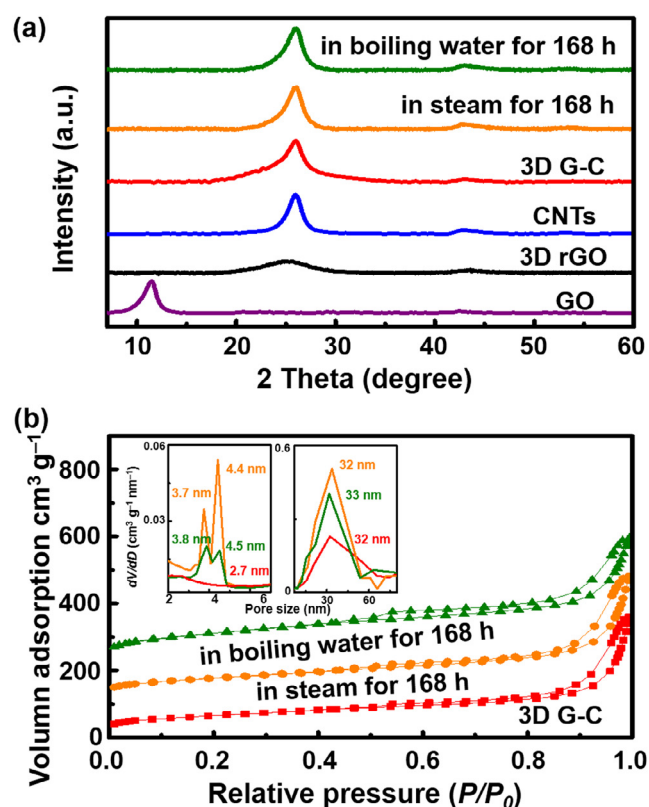


**Fig. 2.** (a) XRD patterns of GO, 3D rGO, CNTs, 3D G-C, and 3D G-C after treatment in steam and treatment in boiling water for 168 h, respectively. (b) The nitrogen adsorption-desorption curves of 3D G-C, 3D G-C after treatment in steam and treatment in boiling water for 168 h, respectively. The isotherms after treatment in steam and treatment in boiling water for 168 h were offset by  $100 \text{ cm}^3 \text{g}^{-1}$  and  $200 \text{ cm}^3 \text{g}^{-1}$ , respectively, at the beginning for clarity. The corresponding pore size distribution curve (insert) is from bottom to up. (c,d) SEM images of 3D G-C after treatment in steam and treatment in boiling water for 168 h, respectively.

images indicated that treated 3D rGO is stacked into thick sheets without a foam structure (Fig. S3e,f).  $N_2$  adsorption–desorption isotherms of 3D G-C were shown in Fig. 2(b). According to the calculation of the BJH formula, the pore size distribution of 3D G-C is mainly concentrated at 2.7 and 32.1 nm, referring to the inner pores of CNTs and secondary pores of G/CNTs assemblies. This hierarchically dual-mesoporous and microporous structure leads to a high specific surface area ( $229 \text{ m}^2 \text{ g}^{-1}$ ) of 3D G-C composite. The hydrothermal water and steam treatments were employed to test the structural stability. The hybrids retain their 3D morphology and structure without any collapse after treatment in steam (Fig. 2c) or treatment in boiling water (Fig. 2d), even for 168 h (Fig. S6 shows the SEM images of 3D G-C every 24 h). Moreover, the XRD patterns (Fig. 2a) of hydrothermally treated 3D G-C hybrids show no change, and very little change of the mesoporous structure and the specific surface area ( $271 \text{ m}^2 \text{ g}^{-1}$  and  $291 \text{ m}^2 \text{ g}^{-1}$ , respectively) in Fig. 2(b). Notably, the assembled pore size distribution of 3D G-C hybrids still remains at  $\sim 32 \text{ nm}$  after hydrothermal treating, while the small increase of the inner pore size of the CNTs may be attributed to the eliminating of the amorphous carbon phase [26]. The high stability of the hybrids is directly attributed to the strong integrated between the graphene nanosheets and CNTs, which is consistent with the TEM observation results.

Firstly, the evidence of  $sp^3$  carbon can be detected by X-ray photoelectron spectroscopy (XPS). As exhibited in Figs. S7 and S8, the C 1s spectra of as-prepared materials can be fitted by five peaks:  $sp^2$  (284.6 eV, the calibration of C 1s peak),  $sp^3$  (285.0 eV), C–O (286.1 eV), C = O (288.9 eV) and a  $\pi$ - $\pi^*$  shake-up feature (292.1 eV) [27–29]. Notably, the peak area ratio of  $sp^3/sp^2$  of 3D G-C is  $0.94 \pm 0.02$ , which is 2.5 times that of mixed G-C ( $0.38 \pm 0.02$ ) (Fig. 3a), 2.4 times that of 3D rGO ( $0.39 \pm 0.02$ ) and 2.5 times that of CNTs ( $0.38 \pm 0.02$ ) (Fig. S9). This is due to the fact that the amount of  $sp^3$ -like carbons is significantly increased. Secondly, the Raman spectra were employed to further confirm that the (D peak) (defect, irregularly arranged and  $sp^3$  carbon) has increased in the 3D G-C hybrids (Fig. 3b and Fig. S10a). Obviously, the Raman spectra of the four samples show two strong peaks at  $1322 \text{ cm}^{-1}$  (D peak) and  $1583 \text{ cm}^{-1}$  (G peak). It is noteworthy that the intensity ratio of the D band and G band ( $I_D/I_G$ , the average of three measurements) of 3D G-C is  $1.32 \pm 0.02$ , which is higher than that of the mixed G-C ( $1.20 \pm 0.02$ ), 3D rGO ( $1.18 \pm 0.02$ ) and CNTs ( $1.18 \pm 0.02$ ) [30–32]. This result revealed that the degree of defect, irregularly arranged and  $sp^3$  carbon in 3D G-C is higher, which is consistent with the increase of the  $sp^3$  carbon of XPS result. Thirdly, the solid-state  $^{13}\text{C}$  NMR spectrum of the 3D G-C hybrids (Fig. 3c) provides a direct evidence of the  $sp^3$  carbon. Two bands, near 118 ppm and 14 ppm, are due to  $sp^2$ -hybridized and  $sp^3$ -hybridized carbon, respectively [33]. The mixed G-C exhibits only one clear band near 118 ppm, characteristic of  $sp^2$ -hybridized carbon and a very weak band near 14 ppm. Moreover, as shown in Fig. S10(b), there is a significant reduction to the peak ( $1385 \text{ cm}^{-1}$ ) of the in-plane bending vibration of O–H in carboxyl groups of 3D G-C, comparing with GO and CNT, probably due to the reaction of –OH and the carboxyl groups and the formation of bonding [34].

From the above, it suggests that  $sp^3$ -like defect structure is generated in the hybrids of graphene and CNTs, which generated excellent stability in structure. Besides, the ratios of  $sp^2/sp^3$  carbon detected by XPS, Raman, and NMR are different, due to the different technological principles and detection positions. These interesting differences further demonstrate the unique 3D structure and  $sp^3$ -like defect structure. The higher surface  $sp^3$  hybridization tested by XPS suggests that  $sp^3$  structure definitely occur on the surface graphene coating because of the high oxygen-containing groups. The obvious increasing intensity of the D band of the ratio of  $I_D/I_G$  in Raman is attributed to formation of the new  $sp^3$  structure. The clear peak of  $sp^3$  carbon in 3D G-C hybrids from the

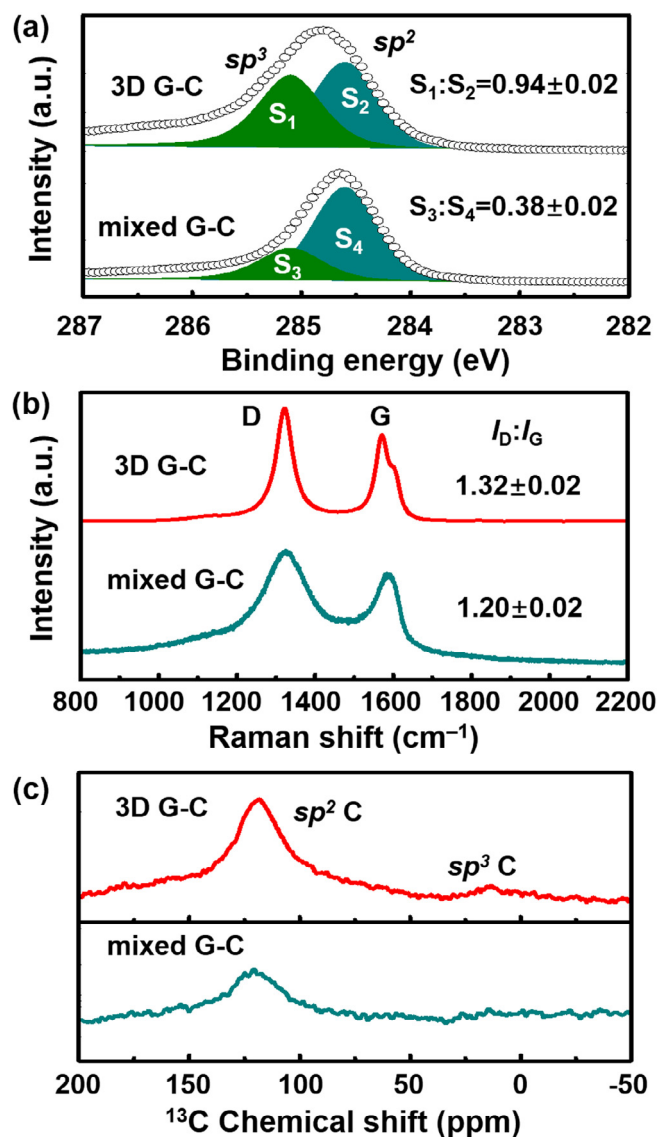
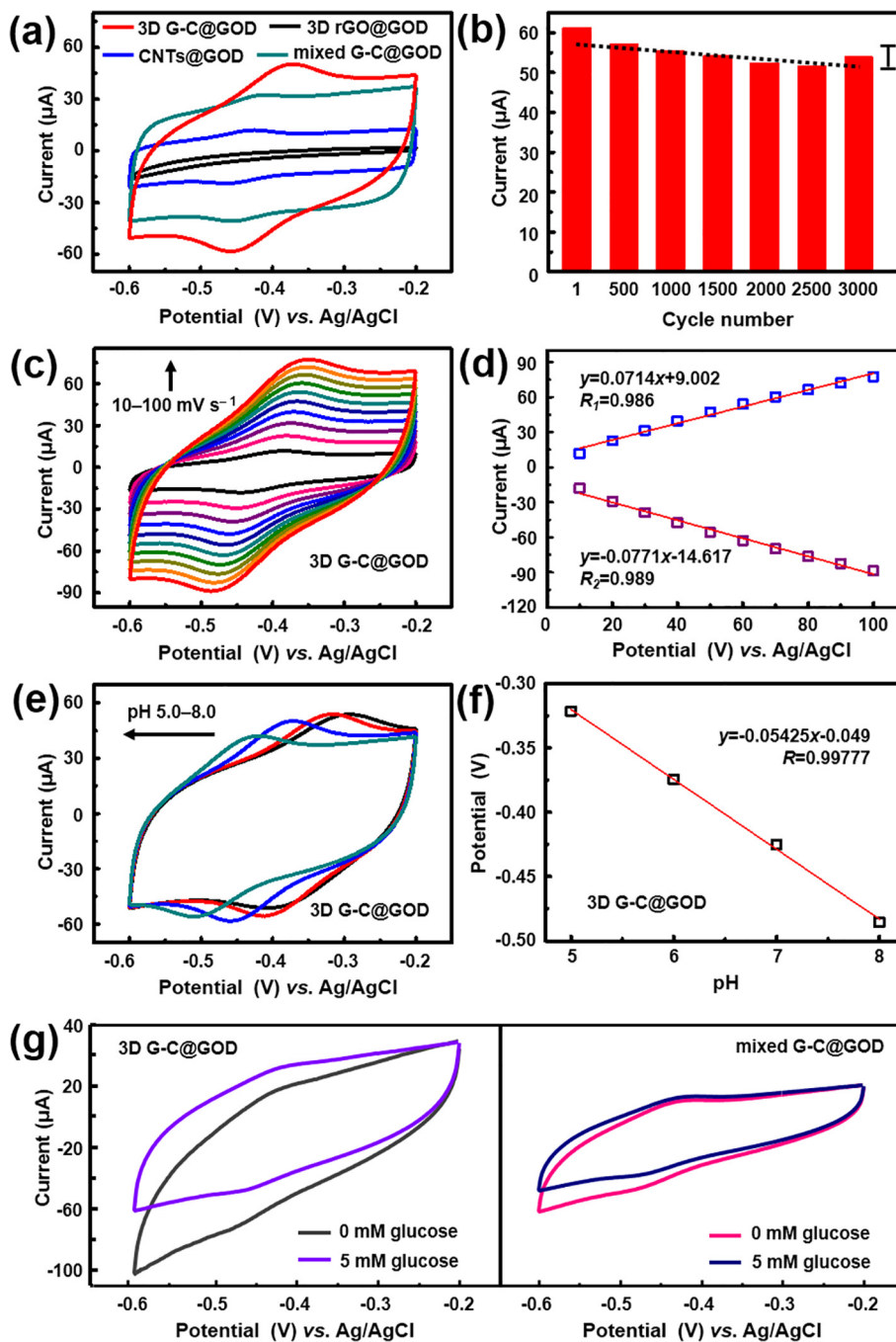


Fig. 3. (a) High-resolution spectra of C 1s ( $sp^2$  C and  $sp^3$  C) of 3D G-C and mixed G-C. (b) Raman spectra of 3D G-C and mixed G-C (the value of  $I_D/I_G$  is the average of three measurements and the standard error and deviation is  $\pm 0.02$ ). (c)  $^{13}\text{C}$  NMR spectra of 3D G-C and mixed G-C.

NMR data is solid proof of  $sp^3$ -like defect structure, and mixed G-C is mainly composed of  $sp^2$  carbon, together with the presence of defects.

Furthermore, activity and stability of bio-electrocatalysis using glucose oxidase (GOD) as model supported on CNTs (CNTs@GOD), graphene (3D rGO@GOD), mixtures of CNTs and graphene (mixed G-C@GOD) and 3D G-C (3D G-C@GOD) have been thoroughly evaluated (Fig. 4). The UV–vis absorption spectra (Fig. S11) indicate that the GOD has been adsorbed in the 3D G-C hybrids. The bio-electrode of 3D G-C@GOD (Fig. 4a) displays the largest electrochemical specific area and the highest peak current ( $50.2 \mu\text{A}$ ); *i.e.* 4.0 folds higher than CNTs@GOD and 1.5 folds higher than mixed G-C@GOD. All electrodes without GOD do not display any peaks, indicating that the reaction peaks are attributed to GOD (Fig. S12a). A long-term stability of 3D G-C hybrids can be seen in Fig. 4(b), which retains 88% of its performance even after 3000 cycles. Additionally, with the scan rate increased from 10 to  $100 \text{ mV s}^{-1}$ , the peak current values of the CV curves were also gradually improved (Fig. 4c). Furthermore, oxidation peak current



**Fig. 4.** (a) Cyclic voltammetry (CV) curves of 3D rGO@GOD, CNTs@GOD, mixed G-C@GOD, 3D G-C@GOD. (b) Peak currents of 3D G-C@GOD at 1st, 500th, 1000th, 1500th, 2000th, 2500th, 3000th cycles. (c) CV curves of 3D G-C@GOD at various scan rates of 10, 20, 30, 40, 50, 60, 70, 80, 90, 100  $\text{mV s}^{-1}$ . (d) Plot of  $I_p$  vs. scan rate ( $v$ ). (e) CV curves of 3D G-C@GOD at pH 5.0, 6.0, 7.0, 8.0 from right to left respectively. (f) Plot of  $E_0$  vs. pH. (g) The CV curves of 3D G-C@GOD and mixed G-C@GOD with 0 mM glucose and 5 mM glucose in an  $\text{O}_2$  state phosphate buffer solution, respectively. The CV tests were in a 0.1 M, pH = 7 phosphate buffer solution.

( $I_{pa}$ ) and reduction peak current ( $I_{pc}$ ), increased linearly with the scan rate ( $v$ ), respectively (Fig. 4d). This quasi-reversible surface controlled electrochemical process indicates that the enzyme-generated electrons fully transfer to the electrode surface [35,36]. Subsequently, the effect of pH value (from 5.0 to 8.0) on the electrochemical performance of electrode was studied. As shown in Fig. 4(e), as the pH value increased, the positions of the cathodic peak and anodic peak move toward the low voltage direction, and the slope value of  $E^0$  vs. pH is about  $-54.3 \text{ mV pH}^{-1}$  (Fig. 4f), which is close to the theoretical value of the Nernstian equation ( $-59.2 \text{ mV pH}^{-1}$ ) for the same number of proton and electron transfer processes, revealing that two protons and two electrons partic-

ipate in the aforementioned electron transfer process [37,38]. Meanwhile, the electrocatalytic response currents of 3D G-C is  $41.1 \mu\text{A}$  towards 5 mM glucose, which is 2.9 folds than that of mixed G-C@GOD ( $14.0 \mu\text{A}$ ) (Fig. 4g) and 2.1 folds than that of CNTs@GOD ( $20.0 \mu\text{A}$ ) (Fig. S13). However, the electrode of 3D G-C without GOD has no response to 5 mM glucose in Fig. S12(b), indicating that the response current is derived from the oxidation of the substrate by GOD.

In addition, the prepared 3D G-C is also a great conductive carrier for sulfur (S). After melting with S, the S-containing materials are named as S@3D G-C (Fig. S14), S@mixed G-C, S@CNTs, S@3D rGO; the S content of the as-prepared cathode materials is about

70 wt% (Fig. S15). Employing these cathode materials to prepare cathode and assembled with lithium metal to form a battery to evaluate the electrochemical performance of S@3D G-C, S@mixed G-C, S@3D rGO and S@CNTs composites. As exhibited in Fig. 5(a), the S@3D G-C cathodic cell shows a typical cyclic voltammetry (CV) curves with two cathodic peaks at 2.30 V and 2.05 V and an anodic peak at 2.40 V. Particularly, the two cathodic peaks can be attributed to a two-step reduction ( $S_8 \rightarrow Li_2S_x$ ,  $x = 4-8$  and  $Li_2S_x \rightarrow Li_2S_2$ ,  $Li_2S_4$ ,  $x = 4-8$ ) during the discharge process and the anodic peak is related to the oxidation of polysulfides to sulfide [39–41]. The three curves are overlapping with the initial cycles, confirming the excellent cyclic stability and highly reversible redox reaction. The electrode of S@3D G-C reveals the best electrochemical rate performance with high capacities of 1261, 957, 778, 698, and 569  $mA h g^{-1}$  at various current densities of 0.1, 0.2, 0.5, 1.0, and 3.0 C, respectively (Fig. 5b). Notably, when the current density recovers to 0.1C, a high capacity of 1055  $mA h g^{-1}$  can be recovered. The charge/discharge platforms under high rates are still obvious and the platform voltages have not changed significantly compared with those of low rate, and all the platform voltages are consistent with the CV curves (Fig. S16). In addition, the typical discharge/charge plateau of the S@3D G-C electrode observed at 3.0 C indicated that faster  $Li^+$  ion diffusion in a 3D structure and less electrochemical polarization, in comparison with the S@3D rGO, S@CNTs and S@mixed G-C [42–44]. Furthermore, electrodes of S@3D G-C demonstrate a high initial discharge capacity of 1300  $mA h g^{-1}$  at 0.2 C (Fig. 5c), corresponding to 77.8% of the theoretical capacity

of sulfur (1672  $mA h g^{-1}$ ), which is 1.7 folds that of mixed G-C (46.8%), 1.9 folds that of CNTs (41.9%), and 1.7 folds that of 3D rGO (44.6%). After 100cycles at 0.2C, the S@3D G-C cathodic cell delivers the highest capacity of 728  $mA h g^{-1}$ , which is much higher than that of S@mixed G-C, S@CNTs, and S@3D rGO (up to 246  $mA h g^{-1}$ ) obtained under the same conditions. This is directly related to the 3D G-C core-shell structure for restraining the shuttle effect of polysulfide [45–47]. And the S@3D G-C electrode also displays a stable cycling performance at a high current density of 1.0 C with high capacity retention about 94% from 250 to 300cycles (Fig. 5d). To analyze the origin of the excellent electrochemical properties of S@3D G-C, electrochemical impedance spectroscopy (EIS) was employed. As shown in Fig. S17, S@3D G-C exhibits the lowest surface contact resistance in contrast to S@mixed G-C, S@CNTs and S@3D rGO after cycling, demonstrating that a better interface resulting of nanofusion in 3D G-C. These observations indicate that our 3D G-C network structure is a highly efficient and stable system as cathode electrodes in Li-S batteries (Table S1). Notably, the presence of  $sp^3$ -like defect interface structure provides the strong interaction at atom level, which facilitates the electron transport. While the 3D structured mixed G-C shows relative low performances in electro-catalysis. This indicates that the  $sp^3$ -like defect structure is an advantageous feature for electron transport and corresponding performance of electro-catalysis.

A formation mechanism of the 3D neural-like structure is proposed in Fig. 6(a). GO acts as a joint center to assemble with several CNTs because of its rich oxygen-containing groups, and these pri-

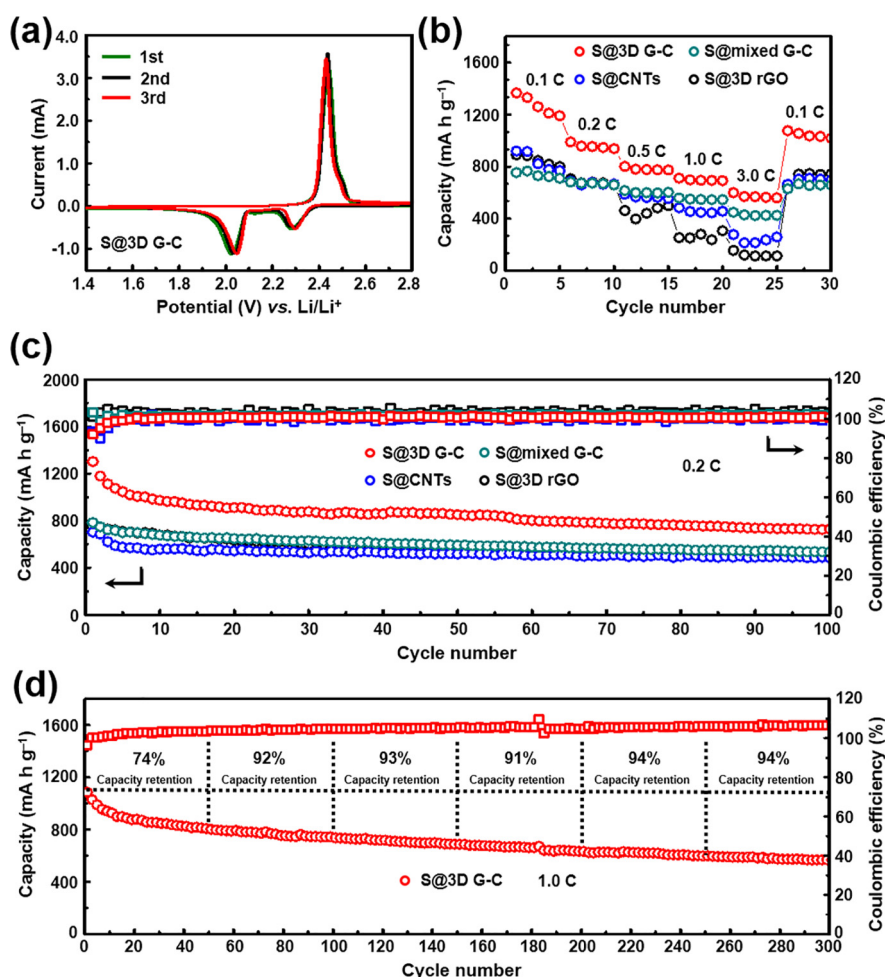


Fig. 5. (a) 1st–3rd CV curves of S@3D G-C at a scan rate of 0.2 mV s<sup>-1</sup>. (b) The rate performance of S@3D G-C, S@mixed G-C, S@CNTs and S@3D rGO at various current densities. (c) Cyclic performance of S@3D G-C, S@mixed G-C, S@CNTs, S@3D rGO at 0.2 C. (d) Long-term cycle performance at 1 C of S@3D G-C.

many units of GO and CNTs might self-assemble into a 3D interconnected network by supramolecular interactions. During hydrothermal treatment, oxygen-containing groups in GO would react and bond with CNTs. With time prolongation under the hydrothermal reaction, the number of bridged bonding increases, resulting in folding of the graphene and CNTs and corresponding  $sp^3$ -like defect

structure. With the fixation of the folding, a new fold  $sp^3$ -like defect structure is formed. Finally, a stable 3D neural-like network structure appears. There are several advantageous features of the synergistic effect in 3D G-C hybrids. Firstly, structural effect is that the 3D neural network structure is similar to the brain, which is a high-efficiency system of a 3D cascade charge transport/collection

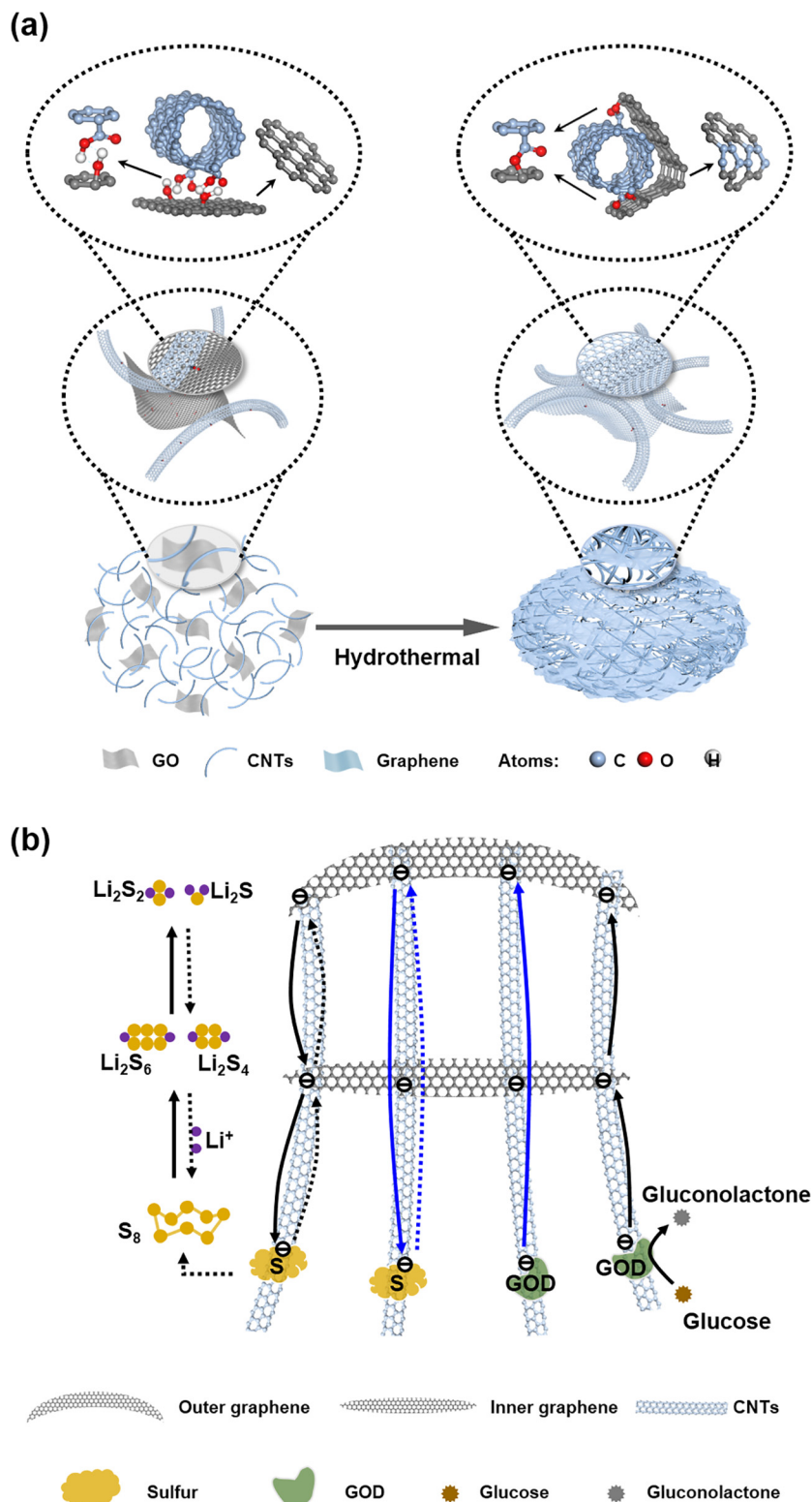


Fig. 6. (a) Schematic illustration of the synthesis of 3D G-C hybrids. (b) Schematic description of the transfer and electrochemical catalysis in a 3D neural-like network of 3D G-C.

[4,6]. Secondly, confined effect is that the core–shell porous structure can prevent the catalytic sites from leaching and the multiple-level pores can highly disperse the catalytic sites [48,49]. Finally, interfacial effect shows that the  $sp^3$ -like defect interface structure is mostly important, because this interface structure not only form the neural-like structure for cascade charge transport, and fabricate the core–shell structure for efficient confinement catalysis, but also provide strong linkage between the rGO and CNTs for highly structural stability, high conductivity and fast interface carries transport [32,50].

Taking this into account, we propose a possible mechanism for the electronic transport, collection and utilization of the heterostructure between graphene and CNTs in 3D G-C hybrids (Fig. 6b). When the Li-S electrodes discharge, the electrons pass through the outer graphene shell to transfer to the CNTs and inner graphene, which act as joint points for further electron transport and reaction with the inner sulfur. During the reaction, the sulfur is reduced to long-chain lithium polysulfides ( $Li_2S_x$ ,  $x = 4-8$ ) at higher potential, and later to short-chain  $Li_2S_2/Li_2S$  at a lower potential. The reversible process occurs when the Li-S electrodes charge. Similarly, the electrons produced by enzymatic oxidation of glucose move to the CNTs, and transport through the inner graphene joint to the outer graphene shell for collection and utilization. The rGO sheets cover around the compositions of rGO and CNTs also can prevent the active sites (such as enzymes and sulfur) from leaching and also collect the carries. Based on the optimized design, the prepared 3D G-C hybrid has an excellent electron transmission network and a stable structure, which is an ideal conductive carrier for enzymes and S. Therefore, whether it is used as an enzyme's carrier for bio-electrocatalysis or as a sulfur carrier for Li-S batteries, the composite materials show excellent electrochemical performance. This result also provides valuable reference for the design of conductive carrier materials in the future.

#### 4. Conclusions

In summary, our investigations obviously suggest that the 3D structure of 3D G-C can not only effectively confine and utilize active sites (such as enzyme and the sulfur); also the neural-like intercross with  $sp^3$ -like defect structure offers high conductivity and a fast carrier transfer. As formation mechanism for the integration of graphene and CNTs, it has been proposed that during the hydrothermal treatment, rich oxygen-containing groups in GO would react and bond with CNTs, forming  $sp^3$ -like defect structure in folded interface region which are viewed as the basis for the demonstrated, enhancing carrier transfer and stability. Our work opens a door to neural-like structured hybrids of nanocarbons with outstanding performance for practical applications and also contributes to a fundamental aspect of the nature of nanocarbon interactions.

#### Declaration of Competing Interest

The authors declare that they have no known competing financial interests or personal relationships that could have appeared to influence the work reported in this paper.

#### Acknowledgments

We acknowledge a joint National Natural Science Foundation of China-Deutsche Forschungsgemeinschaft (NSFC-DFG) project (NSFC grant 51861135313, DFG JA466/39-1). This work also was supported by National Natural Science Foundation of China (21706199), International Science & Technology Cooperation Pro-

gram of China (2015DFE52870) and Jilin Province Science and Technology Development Plan (20180101208JC).

#### Appendix A. Supplementary data

Supplementary data to this article can be found online at <https://doi.org/10.1016/j.jechem.2020.09.020>.

#### References

- [1] C.J. Shearer, A. Cherevan, D. Eder, *Adv. Mater.* 26 (2014) 2295–2318.
- [2] Q. Wang, J. Yan, Z.J. Fan, *Energy Environ. Sci.* 9 (2016) 729–762.
- [3] M.M. Titirici, R.J. White, N. Brun, V.L. Budarin, D.S. Su, F. del Monte, J.H. Clark, M.J. MacLachlan, *Chem. Soc. Rev.* 44 (2015) 250–290.
- [4] Y.L. Bai, Y.S. Liu, C. Ma, K.X. Wang, J.S. Chen, *ACS Nano* 12 (2018) 11503–11510.
- [5] A.M. Cassell, H.T. Ng, L. Delzeit, Q. Ye, J. Li, J. Han, M. Meeyappan, *Appl. Catal., A* 254 (2003) 85–96.
- [6] M.V. Escarcega-Bobadilla, G.A. Zelada-Guillen, S.V. Pyrlin, M. Wegrzyn, M.M. Ramos, E. Gimenez, A. Stewart, G. Maier, A.W. Kleij, *Nat. Commun.* 4 (2013) 2648.
- [7] W. Zhang, H. Xie, R. Zhang, M. Jian, C. Wang, Q. Zheng, F. Wei, Y. Zhang, *Carbon* 86 (2015) 358–362.
- [8] I.A. Kinloch, J. Suhr, J. Lou, R.J. Young, P.M. Ajayan, *Science* 362 (2018) 547–553.
- [9] R. Paul, F. Du, L. Dai, Y. Ding, Z.L. Wang, F. Wei, A. Roy, *Adv. Mater.* 31 (2019) 1805598.
- [10] Z. Yang, J. Tian, Z. Yin, C. Cui, W. Qian, F. Wei, *Carbon* 141 (2019) 467–480.
- [11] D. Jariwala, V.K. Sangwan, L.J. Lauhon, T.J. Marks, M.C. Hersam, *Chem. Soc. Rev.* 42 (2013) 2824–2860.
- [12] X. Jiang, J. Zhao, Y.L. Li, R. Ahuja, *Adv. Funct. Mater.* 23 (2013) 5846–5853.
- [13] H. Hiura, T.W. Ebbesen, J. Fujita, K. Tanigaki, T. Takada, *Nature* 367 (1994) 148–150.
- [14] M. Varga, T. Izak, V. Vretenar, H. Kozak, J. Holovsky, A. Artemenko, M. Hulman, V. Skakalova, D.S. Lee, A. Kromka, *Carbon* 111 (2017) 54–61.
- [15] W. Gao, L.B. Alemany, L. Ci, P.M. Ajayan, *Nat. Chem.* 1 (2009) 403–408.
- [16] Y. Zhou, Q. Bao, L.A.L. Tang, Y. Zhong, K.P. Loh, *Chem. Mater.* 21 (2009) 2950–2956.
- [17] Q. Deng, P. Huang, W.X. Zhou, Q. Ma, N. Zhou, H. Xie, W. Ling, C.J. Zhou, Y.X. Yin, X.W. Wu, X.Y. Lu, Y.G. Guo, *Adv. Energy Mater.* 7 (2017) 1700461.
- [18] H.J.W. S. O.R. E, *J. Am. Chem. Soc.* 131 (1958) 1339–1339.
- [19] Y. Zhu, S. Murali, W. Cai, X. Li, J.W. Suk, J.R. Potts, R.S. Ruoff, *Adv. Mater.* 22 (2010) 3906–3924.
- [20] S.M. Wu, X.L. Liu, X.L. Lian, G. Tian, C. Janiak, Y.X. Zhang, Y. Lu, H.Z. Yu, J. Hu, H. Wei, H. Zhao, G.G. Chang, G. Van Tendeloo, L.Y. Wang, X.Y. Yang, B.L. Su, *Adv. Mater.* 30 (2018) 1802173.
- [21] Y. Lu, X. Cheng, G. Tian, H. Zhao, L. He, J. Hu, S.M. Wu, Y. Dong, G.G. Chang, S. Lenaerts, S. Siffert, G. Van Tendeloo, Z.F. Li, L.L. Xu, X.Y. Yang, B.L. Su, *Nano Energy* 47 (2018) 8–17.
- [22] H. Sun, Y. Wang, S. Liu, L. Ge, L. Wang, Z. Zhu, S. Wang, *Chem. Comm.* 49 (2013) 9914–9916.
- [23] T.F. Yeh, J.M. Syu, C. Cheng, T.H. Chang, H. Teng, *Adv. Funct. Mater.* 20 (2010) 2255–2262.
- [24] X.Y. Yang, A. Vantomme, A. Lemaire, F.S. Xiao, B.L. Su, *Adv. Mater.* 18 (2006) 2117–2122.
- [25] Z.J. Fan, W. Kai, J. Yan, T. Wei, L.J. Zhi, J. Feng, Y.M. Ren, L.P. Song, F. Wei, *ACS Nano* 5 (2011) 191–198.
- [26] I. Janowska, O. Ersen, T. Jacob, P. Vennégues, D. Bégin, M.J. Ledoux, C. Pham Huu, *Appl. Catal., A* 371 (2009) 22–30.
- [27] X.H. Yang, J.W. Guo, S. Yang, Y. Hou, B. Zhang, H.G. Yang, *J. Mater. Chem. A* 2 (2014) 614–619.
- [28] S.W. Lee, N. Yabuuchi, B.M. Gallant, S. Chen, B.S. Kim, P.T. Hammond, Y. Shao Horn, *Nat. Nanotechnol.* 5 (2010) 531–537.
- [29] S.I. Kim, B.B. Sahu, S.E. Kim, A. Ali, E.H. Choi, J.G. Han, *J. Mater. Chem. B* 3 (2015) 3267–3278.
- [30] D. Su, M. Cortie, G. Wang, *Adv. Energy Mater.* 7 (2017) 1602014.
- [31] S. Ma, L. Wang, Y. Wang, P. Zuo, M. He, H. Zhang, L. Ma, T. Wu, G. Yin, *Carbon* 143 (2019) 878–889.
- [32] X. Chen, J. Tao, Y. Liu, R. Bao, F. Li, C. Li, J. Yi, *Carbon* 146 (2019) 736–755.
- [33] P. Duan, X. Li, T. Wang, B. Chen, S.J. Juhl, D. Koeplinger, V.H. Crespi, J.V. Badding, K. Schmidt Rohr, *J. Am. Chem. Soc.* 140 (2018) 7658–7666.
- [34] C. Chung, M. Lee, E. Choe, *Carbohydr. Polym.* 58 (2004) 417–420.
- [35] Y. Yu, Z. Chen, S. He, B. Zhang, X. Li, M. Yao, *Biosens. Bioelectron.* 52 (2014) 147–152.
- [36] K.P. Prasad, Y. Chen, P. Chen, *ACS Appl. Mater. Interfaces* 6 (2014) 3387–3393.
- [37] Z. Kang, K. Jiao, J. Cheng, R. Peng, S. Jiao, Z. Hu, *Biosens. Bioelectron.* 101 (2018) 60–65.
- [38] M. Christwardana, Y. Chung, Y. Kwon, *Nanoscale* 9 (2017) 1993–2002.
- [39] A. Abdul Razzaq, Y. Yao, R. Shah, P. Qi, L. Miao, M. Chen, X. Zhao, Y. Peng, Z. Deng, *Energy Storage Mater.* 16 (2019) 194–202.
- [40] T. Chen, Z. Zhang, B. Cheng, R. Chen, Y. Hu, L. Ma, G. Zhu, J. Liu, Z. Jin, *J. Am. Chem. Soc.* 139 (2017) 12710–12715.
- [41] Z. Li, Z. Xiao, S. Wang, Z. Cheng, P. Li, R. Wang, *Adv. Funct. Mater.* 29 (2019) 1902322.

- [42] H.J. Peng, J.Q. Huang, M.Q. Zhao, Q. Zhang, X.B. Cheng, X.Y. Liu, W.Z. Qian, F. Wei, *Adv. Funct. Mater.* 24 (2014) 2772–2781.
- [43] C. Tang, Q. Zhang, M.Q. Zhao, J.Q. Huang, X.B. Cheng, G.L. Tian, H.J. Peng, F. Wei, *Adv. Mater.* 26 (2014) 6100–6105.
- [44] M. Yan, H. Chen, Y. Yu, H. Zhao, C.F. Li, Z.Y. Hu, P. Wu, L. Chen, H. Wang, D. Peng, H. Gao, T. Hasan, Y. Li, B.L. Su, *Adv. Energy Mater.* 8 (2018) 1801066.
- [45] H. Al Salem, G. Babu, C.V. Rao, L.M. Arava, *J. Am. Chem. Soc.* 137 (2015) 11542–11545.
- [46] G. Zheng, Y. Yang, J.J. Cha, S.S. Hong, Y. Cui, *Nano Lett.* 11 (2011) 4462–4467.
- [47] Q. Zhao, K. Zhao, G. Ji, X. Guo, M. Han, J. Wen, Z. Ren, S. Zhao, Z. Gao, R. Wang, M. Li, K. Sun, N. Hu, C. Xu, *Chem. Eng. J.* 361 (2019) 1043–1052.
- [48] G. Gnana Kumar, S.H. Chung, T. Raj Kumar, A. Manthiram, *ACS Appl. Mater. Interfaces* 10 (2018) 20627–20634.
- [49] L. Sun, M. Li, Y. Jiang, W. Kong, K. Jiang, J. Wang, S. Fan, *Nano Lett.* 14 (2014) 4044–4049.
- [50] L. Peng, Y. Feng, P. Lv, D. Lei, Y. Shen, Y. Li, W. Feng, *J. Phys. Chem. C* 116 (2012) 4970–4978.